SCIENTIFIC REP⚙RTS

OPEN

Microbial fuel cell assisted band gap narrowed TiO$_2$ for visible light-induced photocatalytic activities and power generation

Mohammad Ehtisham Khan[1], Mohammad Mansoob Khan [ID][2], Bong-Ki Min[3] & Moo Hwan Cho [ID][1]

This paper reports a simple, biogenic and green approach to obtain narrow band gap and visible light-active TiO$_2$ nanoparticles. Commercial white TiO$_2$ (*w*-TiO$_2$) was treated in the cathode chamber of a Microbial Fuel Cell (MFC), which produced modified light gray TiO$_2$ (*g*-TiO$_2$) nanoparticles. The DRS, PL, XRD, EPR, HR-TEM, and XPS were performed to understand the band gap decline of *g*-TiO$_2$. The optical study revealed a significant decrease in the band gap of the *g*-TiO$_2$ (E$_g$ = 2.80 eV) compared to the *w*-TiO$_2$ (E$_g$ = 3.10 eV). The XPS revealed variations in the surface states, composition, Ti^{4+} to Ti^{3+} ratio, and oxygen vacancies in the *g*-TiO$_2$. The Ti^{3+} and oxygen vacancy-induced enhanced visible light photocatalytic activity of *g*-TiO$_2$ was confirmed by degrading different model dyes. The enhanced photoelectrochemical response under visible light irradiation further supported the improved performance of the *g*-TiO$_2$ owing to a decrease in the electron transfer resistance and an increase in charge transfer rate. During the TiO$_2$ treatment process, electricity generation in MFC was also observed, which was ~0.3979 V corresponding to a power density of 70.39 mW/m^2. This study confirms narrow band gap TiO$_2$ can be easily obtained and used effectively as photocatalysts and photoelectrode material.

Since 1972, titanium dioxide (TiO$_2$) has been recognized as a potential photocatalyst by researcher's worldwide[1]. TiO$_2$ nanocrystals are well-known semiconductors that can catalyze solar powered reactions, such as water splitting, catalysis, photocatalysis, and environmental remediation[2–5]. On the other hand, TiO$_2$ mainly absorbs light in the UV part of the solar spectrum; therefore, researchers hope that lowering its band gap energy will also enable it to absorb visible and infrared light[4–9].

Previously studies have reduced the band gap of TiO$_2$ by doping it with metals or non-metals, wrapping it with graphene, or introducing intrinsic defects into the TiO$_2$ crystals[10–22]. These methods somehow increase the amount of partial visible light absorption but complete visible light and infrared light absorption is not achieved. Researchers used hydrogenation and other techniques to produce a black, red, blue form of TiO$_2$ by introducing disorder, which absorbs light in the UV, visible and near infrared regions of the spectrum[6–9]. This increases the amount of solar light absorption of the black, red, and blue TiO$_2$, which can be used to generate hydrogen gas and be applied in other visible light-induced applications, such as environmental remediation[6–9,23,24]. Researchers have also found that the hydrogenation process produces disorder in the surface layer of the TiO$_2$ nanocrystals. Based on these studies, researchers have suggested that the hydrogen also 'mops up' broken titanium and oxygen bonds, forming new bonds that lower the band gap to the near infrared region[23–28].

Significant developments in TiO$_2$ photocatalysis and hydrogenation as well as other approaches that are novel and unique, such as surface doping or modification of TiO$_2$, have been made to increase the photocatalytic activity under visible light irradiation[25,26]. Black TiO$_2$ was reported to catalyze the photo-decomposition of organic molecules much better than normal nanophase TiO$_2$[26]. They also found that its ability to catalyze water splitting

[1]School of Chemical Engineering, Yeungnam University, Gyeongsan-si, Gyeongbuk, 38541, South Korea. [2]Chemical Sciences, Faculty of Science, Universiti Brunei Darussalam, Jalan Tungku Link, Gadong, BE, 1410, Brunei Darussalam. [3]Materials Science Centre, Yeungnam University, Gyeongsan-si, Gyeongbuk, 38541, South Korea. Correspondence and requests for materials should be addressed to M.M.K. (email: mmansoobkhan@yahoo.com) or M.H.C. (email: mhcho@ynu.ac.kr)

into hydrogen and oxygen under sunlight was improved greatly. Compared to conventional TiO$_2$ and other metal oxide materials, it exhibits significantly higher efficiency under the same conditions[6].

We previously reported band gap engineered TiO$_2$ nanoparticles using electron beam irradiation which was simple and the reproducibility was quite high. Electron beam irradiated TiO$_2$ nanoparticles showed notable decrease in the band gap as well as enhanced visible light-induced photo-degradation response towards methylene blue (MB) and brilliant blue G (BB) degradation, which was not possible for untreated TiO$_2$ nanoparticles under similar conditions[21]. In the present study, white commercial TiO$_2$ (w-TiO$_2$) was modified (by forming defects) to a light gray colour (g-TiO$_2$) using the cathode chamber of a Microbial Fuel Cell (MFC), which is a green, biogenic, novel and energy efficient process as compared to electron beam irradiation approach. The g-TiO$_2$ showed an absorbance in the visible and near infrared region of the solar spectrum as well as improved visible light-induced photocatalytic and photoelectrochemical performances. The enhanced visible light activities of g-TiO$_2$ might lead to various novel and efficient applications, which will open new horizons for metal oxide nanostructures with different types of defects and narrow band gap energies. Surprisingly, the treatment of TiO$_2$ in the MFC cathode also generated electricity, which is energy efficient. The main difference between electron beam irradiation approach[21] and MFC treatment is that, this approach is environmentally friendly approach which does not involve any external energy, chemicals or doping agents which make this modification method highly economical, simple, green, biogenic, useful, and efficient in the field of band gap engineering of metal oxides and has great potential for real applications in the photodegradation of several toxic dyes.

Results and Discussion

This paper reports a novel and alternative methodology to improve the visible light absorption of w-TiO$_2$ by engineering it and forming different types of disorder. The modification process was achieved in MFC, which can produce an array of defects or disorder in the TiO$_2$ nanoparticles, by this means, imparting novel characteristics, such as a reduced band gap, rapid charge carrier movements, and visible light-induced photocatalytic activities. This easy synthesis procedure does not include any expensive, toxic and hazardous chemicals, which make this modification method highly economical, simple, green, useful, and efficient in the field of band gap engineering of metal oxides. The complete modification process takes place in water at room temperature under atmospheric pressure. Fig. S1 presents the schematic diagram aimed at the modification of commercially obtainable TiO$_2$ nanoparticles in a MFC. The electrons and protons generated in the anode of the MFC can either interact with some of the Ti^{4+} ions and reduce them to Ti^{3+} or interact with the TiO$_2$ surface, which can alter the TiO$_2$ composition[21,29]. The in-situ created species, such as electrons, protons, and Ti^{3+} ions, modified the TiO$_2$ surface, which may impart enhanced visible light induced photocatalytic activities to g-TiO$_2$[21,30,31].

X-ray diffraction studies. The structures of the w-TiO$_2$ and g-TiO$_2$ nanoparticles were examined by XRD in the 10–140° 2θ range. The strong XRD peaks (Fig. 1) indicate that the TiO$_2$ nanoparticles were highly crystalline. The crystalline phase had an anatase and a rutile structure (Table 1) with a mean crystal size of approximately 25 nm, which is in agreement with the HRTEM observations.

The Rietveld refinement was used as a simple tool to verify the precise structure of the w-TiO$_2$ and g-TiO$_2$ nanoparticles and analyse the phase transformation from anatase to rutile. Using this method, the structural compositions of each samples were analysed qualitatively by fitting the experimental powder XRD profiles with respect to corresponding structural parameters (i.e. lattice parameters, atomic coordinates) and instrumental parameters (i.e. zero-point and profile parameters), as shown in Table 1. The refinement was converted to final residual factors (Table S2) of R$_{wp}$ = 7.59 ± 0.3%, R$_{exp}$ = 6.83 ± 0.2% and χ^2 = 1.234 ± 0.2 for w-TiO$_2$ nanoparticles, and R$_{wp}$ = 7.70 ± 0.2%, R$_{exp}$ = 6.69 ± 0.1% and χ^2 = 1.324 ± 0.3 for g-TiO$_2$ nanoparticles. R$_{wp}$ is the weighted-profile R value, R$_{exp}$ is the statistically expected R value, and χ^2 is the goodness of fit (GoF), which is the square of the ratio between R$_{wp}$ and R$_{exp}$. The χ^2 is the goodness of fit values was calculated using given below equation (1). These calculated values of Rietveld refinement further confirmed the changes/modification of the w-TiO$_2$ to g-TiO$_2$ nanoparticles[32].

$$GoF = \frac{\sum_i w_i(y_{io} - y_{ic})^2}{N - P} = \left(\frac{R_{wp}}{R_{exp}}\right)^2$$

(1)

where, N is the number of points and P is the number of parameters.

The Rietveld refinement of the XRD data of the w-TiO$_2$ and g-TiO$_2$ nanoparticles showed that after modification, the phase fraction of anatase of w-TiO$_2$ decreased 1.234 ± 0.2 compared to g-TiO$_2$ nanoparticles, whereas the phase fraction of rutile of w-TiO$_2$ was increased to 1.324 ± 0.3 compared to g-TiO$_2$ nanoparticles. The phase fraction decrease (anatase) and increase (rutile) of g-TiO$_2$ compared to w-TiO$_2$ was attributed to the oxidation state changes from Ti^{4+} to Ti^{3+} which was confirmed from these values (1.234 ± 0.2) and (1.324 ± 0.3). It addition, the phase fraction is also indicated by the unit cell volume of g-TiO$_2$ nanoparticles for the anatase and rutile phase increased ~0.02% and ~0.106% compared to w-TiO$_2$ (Table 1). The increase in the unit cell volume was attributed to the formation of some Ti^{3+} and defects in the sample, which is expected to be responsible for the increase in unit cell volume[21,33]. This XRD technique is incompatible to distinguish the oxidation state changes of two samples. The formation of Ti^{3+} can be easily detected by using EPR analysis (Fig. 2(b)) which is the confirmation of Ti^{3+} formation in gray titania (Fig. 1).

Raman spectroscopy. Raman spectroscopy was performed to observe the variations in the structure and disorder in the g-TiO$_2$ nanoparticles after the introduction of disorder using MFC. The two polymorphs of TiO$_2$ belong to different space groups: D$_{4h}$[19] (I4$_1$/amd) for anatase and D$_{4h}$[14] (P4$_2$/mnm) for rutile, which has distinct characteristics in Raman spectra[6]. For anatase TiO$_2$, there are six Raman active modes with frequencies at 144,
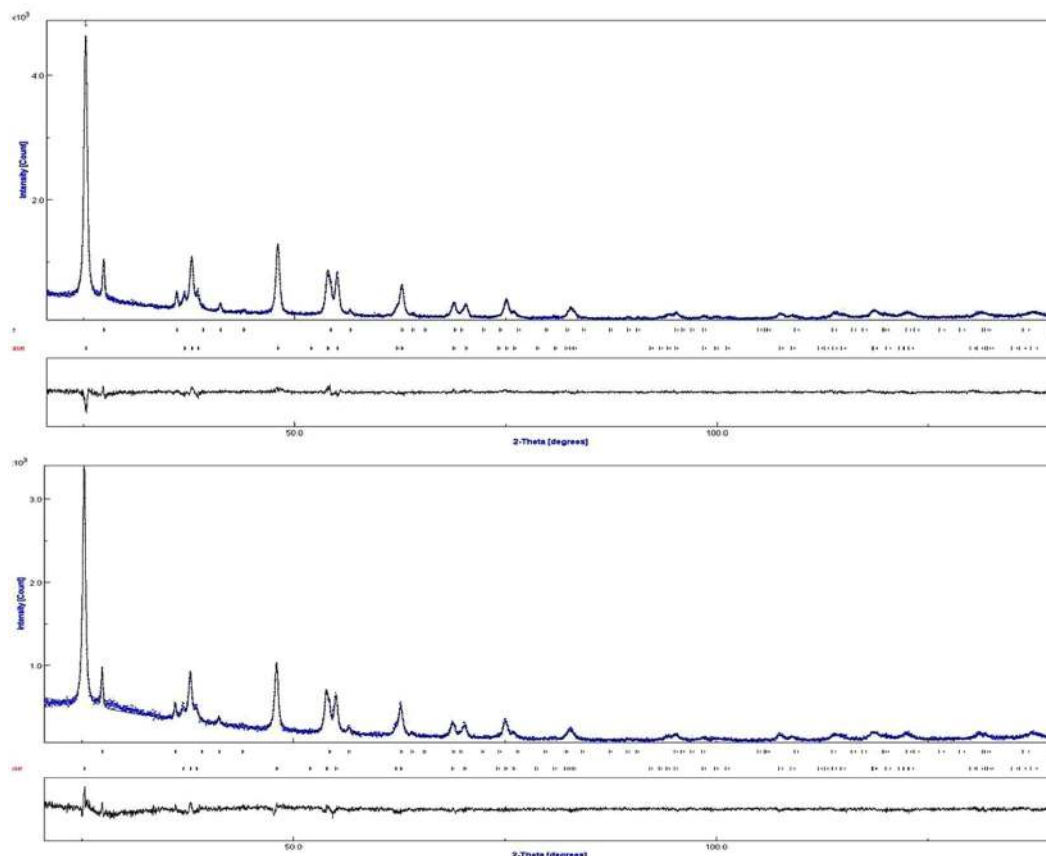
Figure 1. XRD patterns of the (**a**) w-TiO$_2$, and (**b**) g-TiO$_2$ nanoparticles obtained after Rietveld refinement of w-TiO$_2$ and g-TiO$_2$.

Sample	Phase	Phase fraction	Cell parameter(Å)			V(Å^3)
			a	b	c	
w-TiO$_2$	Anatase	0.908	3.7890	3.7890	9.5131	136.58
	Rutile	0.092	4.5989	4.5989	2.9583	62.586
g-TiO$_2$	Anatase	0.901	3.7896	3.7896	9.5127	136.61
	Rutile	0.099	4.5985	4.5985	2.9620	62.635

Table 1. Relevant crystallographic data for w-TiO$_2$ and g-TiO$_2$ nanoparticles established from the powder X-ray diffraction data after Rietveld refinements.

197, 399, 515, 519 (superimposed with the 515 cm^{-1} band), and 639 cm^{-1} [6]. The modified g-TiO$_2$ nanoparticles display the typical anatase Raman bands similar to the w-TiO$_2$ nanoparticles, in addition to the increased intensity peak of the anatase Raman peak (Fig. 2a). The characteristic anatase mode at 144 cm^{-1} was present in both samples (w-TiO$_2$ and g-TiO$_2$) which indicate dominance of the anatase type TiO$_2$ presence in the samples. Das et $al.$[33] and Park et $al.$[34] reported that the intensity of the peak increases with increasing number of non-stoichiometry defects, which increase the light absorption capacity of the TiO$_2$ nanoparticles. Therefore, in the present case the increased intensity of the Raman bands clearly indicates that structural changes have occurred after a treatment in MFC, resulting in formation of some disorder or defects, which were confirmed further by EPR and DRS analysis[21,33–36].

Electron paramagnetic resonance. The EPR spectra of the w-TiO$_2$ and g-TiO$_2$ nanoparticles were recorded (Fig. 2b) at room temperature (RT) and 20 K. The w-TiO$_2$ and g-TiO$_2$ nanoparticles at RT did not show any EPR signals, while the EPR signals for w-TiO$_2$ and g-TiO$_2$ nanoparticles were clear at 20 K. The EPR signal for g-TiO$_2$ at 20 K was much stronger than that of w-TiO$_2$ with a g value of 2.04[28]. The detected g value (Fig. S2) matched the characteristics of the paramagnetic Ti^{3+} ion centre in a distorted rhombic oxygen ligand field. The w-TiO$_2$ showed another EPR signal at 20 K, which corresponds to oxygen vacancies, which was very small, whereas in the case of g-TiO$_2$, this EPR signal appears to overlap with the Ti^{3+} signal, resulting in dramatic enhancement of the peak intensity[8,29,30]. Therefore, EPR showed that g-TiO$_2$ has paramagnetic characteristics
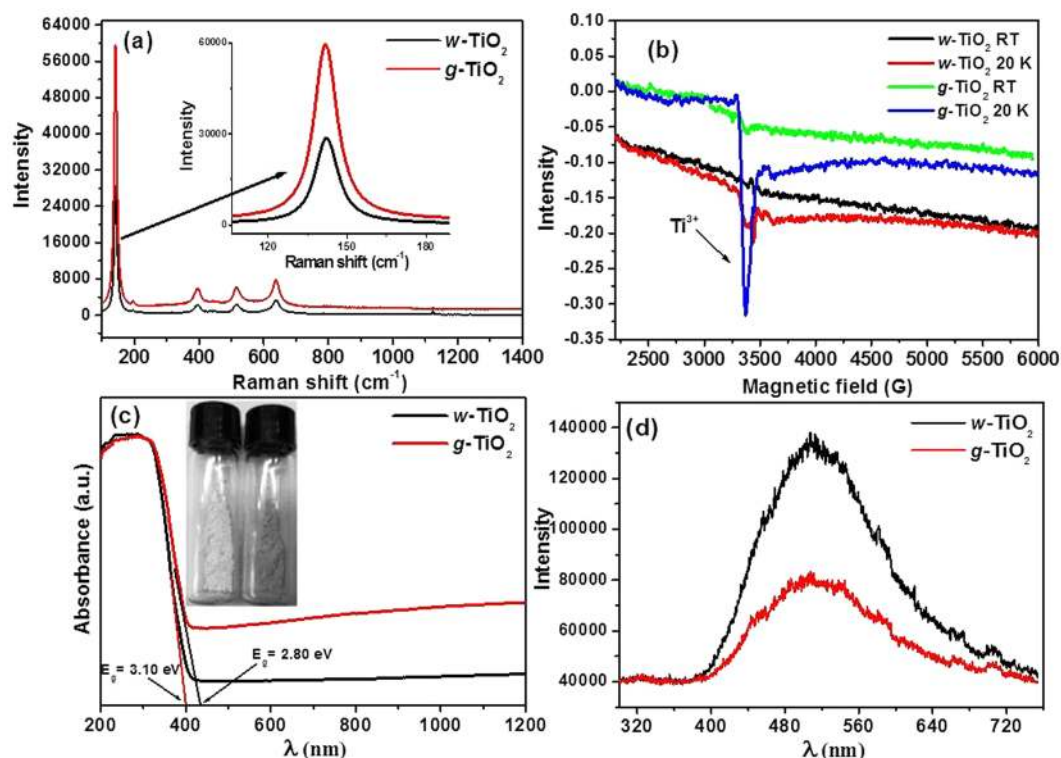
Figure 2. (**a**) Raman spectra, (**b**) EPR spectra at room temperature and 20 K, (**c**) UV-vis diffuse absorbance spectra, and (**d**) PL spectra of the w-TiO$_2$ and g-TiO$_2$ nanoparticles.

and oxygen vacancies, which enhances the visible light-induced photocatalytic activity[8,31,37,38]. Note that EPR is insensitive to Ti^{4+} species; hence, no signal is expected from it. This observation is very useful for identifying the Ti^{3+}-related defects and oxygen vacancies related with Ti^{3+} lattice and F[+] centres[20] (Fig. 2).

UV-vis spectroscopic studies. Figure 2c shows the UV-vis diffuse absorbance spectra, i.e., optical response of the w-TiO$_2$ and g-TiO$_2$ nanoparticles, in which g-TiO$_2$ nanoparticles show higher visible-light absorption than the w-TiO$_2$ nanoparticles. The commercial w-TiO$_2$ nanoparticles only respond to ultraviolet light due to its intrinsic wide band gap. The improvement in the visible-light absorption of g-TiO$_2$ nanoparticles was attributed to two factors: the formation of oxygen vacancies[8,17], and surface disorder[8,16]. Mao *et al*. reported the surface disorder of anatase TiO$_2$ nanoparticles following a hydrogen treatment, which shifted the valence band position by 2.18 eV[16]. In this case, the band gap of w-TiO$_2$ nanoparticles shifted from 3.15 eV to 2.80 eV (Fig. 2c) for g-TiO$_2$ nanoparticles. As a result, the energy gap between the valence band and the conduction band was narrowed dramatically to the point that was small enough for visible-light absorption. Hence, it was attributed to the absorption of visible light because of the formation of oxygen vacancies and other related defects in g-TiO$_2$. The energy levels of the oxygen vacancies are approximately 0.75–1.18 eV below the conduction band of hydrogen-reduced TiO$_2$[8,20]. The visible-light absorption is associated with the transitions from the TiO$_2$ valence band to the oxygen vacancy levels or from the oxygen vacancies to the TiO$_2$ conduction band[20–22]. For the g-TiO$_2$ nanoparticles, which appears to be self-doped Ti^{3+} (Fig. 2(c), red line), the considerably large absorption tail in the visible and NIR regions was observed, which is consistent with the change in colour of the powders from white to gray (Fig. 2c)[8,9,21]. The high absorption tail in the visible and NIR regions also provides clear evidence that the g-TiO$_2$ nanoparticles contain a large number of oxygen vacancies[8,9]. The high absorption tail in the visible and NIR regions also provides clear evidence that the g-TiO$_2$ nanoparticles contain a large number of defects/oxygen vacancies[6,24].

These results also suggest that Ti^{3+} induced visible-light absorption that would have formed an isolated states between the forbidden gap in TiO$_2$, as reported previously, rather than a shift in the position of either band edge, which usually takes place as a result of doping with metals or non-metals[2,12–16,39]. Theoretical studies also confirmed that formation of oxygen vacancies and Ti^{3+} could result in an electronic state vacancy band below the conduction band[8,21].

PL studies. PL was performed to understand the migration, and transfer of charge carriers, efficiency of charge carrier trapping in semiconductor nanostructures. It is well identified that the PL signals of semiconductor materials result from the recombination rate of photo-induced charge carriers. In general, the lower the PL intensity, the lower the recombination rate of photo-induced electron–hole pairs, and the higher the photocatalytic activity of semiconductor photocatalysts[39]. In photoluminescence signals and their intensity are closely related to the improved photocatalytic activity. Further addition or modification in metal NPs reduces the PL intensities, due to shorter distance of inter band metal ions, which result in an energy transfer between nearby
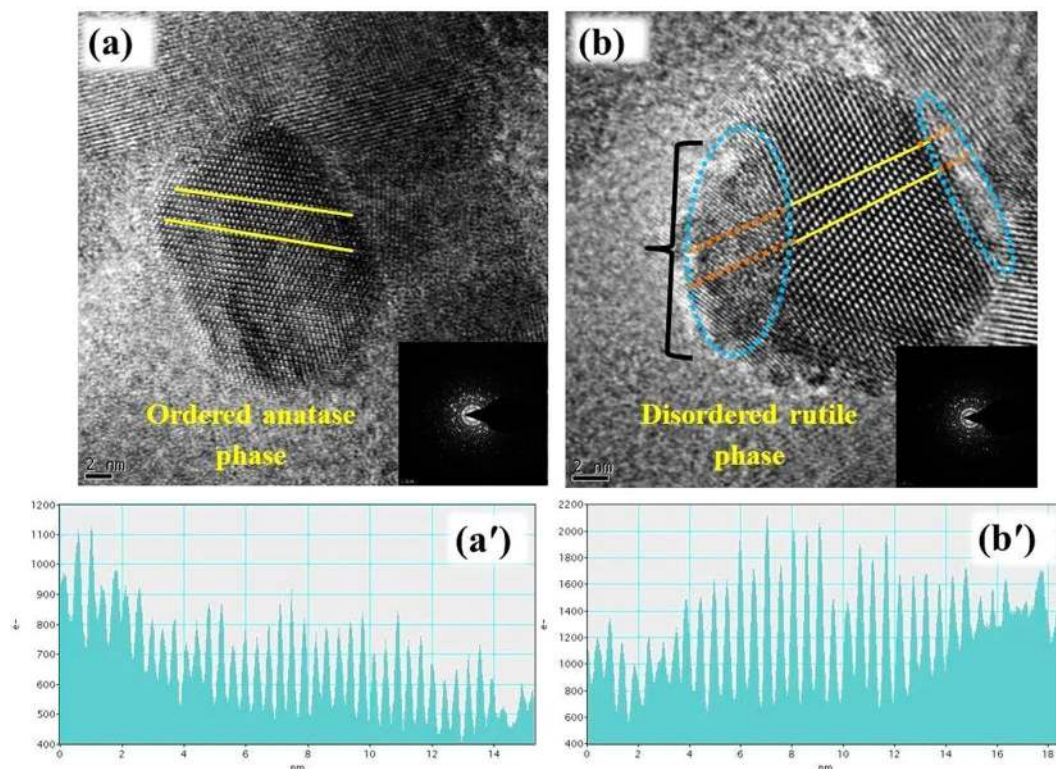
Figure 3. HRTEM image and structural analysis of (**a**) w-TiO$_2$ and (**b**) g-TiO$_2$. The insets in (**a**) and (**b**) show the corresponding selected area electron diffraction pattern. (**a′**) shows line analysis of w-TiO$_2$ and (**b′**) shows line analysis of g-TiO$_2$. The zeros of the axis in (a′) and (b′) correspond to the left ends of the lines in (**a**) and (**b**).

ions. The technique is useful because PL emission occurs mainly through the recombination of free carriers. The PL spectra of semiconductors are related to the transfer behaviour of the photo-induced electrons and holes, and can be used to estimate the recombination rate of charge carriers and understand the fate of electron–hole pairs in semiconductor nanostructures[40,41]. In other words, the PL emission intensity is generally associated with the recombination rate of the photo-induced electrons and holes, in which higher emission intensity reflects the fast recombination rate, whereas a lower intensity reflects the relatively slow recombination rates. This lower recombination may provide large number of charge carriers, which is actively participating in a range of oxidative and reductive photocatalytic degradation reactions of various dyes. As shown in Fig. 2d, the PL emission intensity of w-TiO$_2$ was reduced significantly after inducing defects by MFC, which suggests that the charge carriers are trapped by the defects present in the g-TiO$_2$, which enhances the charge separation efficiency. Different types of defects were reported to greatly affect the PL emission intensity of the metal oxides. For example, Jing *et al.*[39], and Chetri *et al.*[41], reported that the presence of defects quenched the PL signals of metal oxides significantly. Based on the above discussion, it could be concluded that the presence of defects in the g-TiO$_2$ acts as trapping centres, which reduces the emission intensity of the PL signal[40].

Microstructure analysis of w-TiO2 and g-TiO2 nanoparticles.

Figure 3 shows HRTEM images, SAED, and structural analysis of the w-TiO$_2$ and g-TiO$_2$ nanoparticles, which are in the range of 15 to 30 nm and in accordance with XRD analysis. w-TiO$_2$ was completely crystalline, showing clearly-resolved and well-defined lattice fringes, even at the surface of the nanocrystals (Fig. 3a). The distance between the adjacent lattice planes was 0.37 nm, which is typical for anatase, and uniform throughout the whole nanocrystals (Fig. 3a). The measured lattice spacing of 0.37 nm coordinated the distance between the {101} planes of the anatase TiO$_2$ crystal. The reflection from the similar {101} plane was prominent in the XRD patterns (Fig. 1) of the w-TiO$_2$ and g-TiO$_2$ nanoparticles. The spot SAED pattern [inset of Fig. 3(a),(b)] and continuous lattice confirmed the crystalline nature of the w-TiO$_2$ and g-TiO$_2$ nanoparticles. On the other hand, the outer edge of g-TiO$_2$ nanoparticles gives the blurry impression, indicating an amorphous or disorder phase on the nanoparticles surface. The g-TiO$_2$n-anoparticles has a crystalline-disordered structure (Fig. 3b), and the outer layer can be seen readily, which is a structural deviation from the standard crystalline anatase. In contrast, the yellow colour encircled lattice line is disrupted and unclear at the edge of the nanoparticles. The core of the nanoparticles shows a well resolved {101} lattice plane with typical anatase plane distance on the disordered outer layer; the distances between the adjacent lattices planes are no longer uniform (Fig. 3b). This structural difference clearly verifies the disordered crystalline nature of the surface layer of the g-TiO$_2$. Moreover, HRTEM of the w-TiO$_2$ and g-TiO$_2$ nanoparticles did not show any distinct changes in crystallinity (Fig. 3).
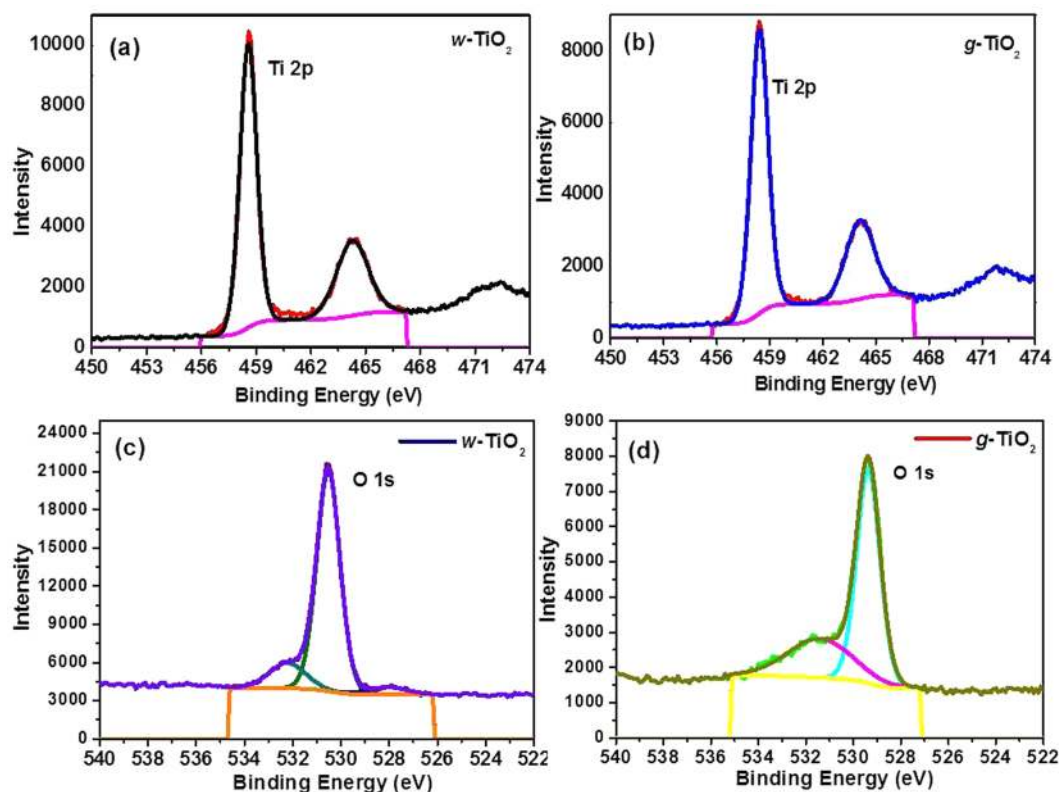
Figure 4. XPS (**a** and **b**) Ti 2p, and (**c** and **d**) O 1 s of the *w*-TiO$_2$ and *g*-TiO$_2$ nanoparticles.

Figure. 3(a′) shows the distance between the adjacent lattice planes, in the nm range, which is characteristic of anatase and uniform throughout the entire nanocrystals spectrum of *w*-TiO$_2$ and (b′) displays a crystalline-disordered core-shell structure for *g*-TiO$_2$ nanoparticles. Fig. S3(a), (b) as well as Fig. S3(a′), (b′) shows the HAADF-STEM images and EDX data of the *w*-TiO$_2$ and *g*-TiO$_2$ nanoparticles. In contrast, the difference between Fig. S3a,b suggests the surface modification of *w*-TiO$_2$ in MFC. This finding was confirmed by SAED (the inset of Fig. 4a,b) and EDX analysis (Fig. S3a′,b′) of different regions of the nanoparticles.

XPS Analysis.   XPS was performed on *w*-TiO$_2$ and *g*-TiO$_2$ nanoparticles for the surface characterization, oxidation states and other observations. C, O, and Ti were noticed in the survey scan spectra (Fig. S4(a) ESI). The C 1 s photoelectron peak (Fig. S4(b) ESI) at a binding energy (BE) of 284.5 eV was stronger for *w*-TiO$_2$ than the *g*-TiO$_2$ nanoparticles, which was ascribed to the elimination of surface carbon impurities from the *g*-TiO$_2$ nanoparticles. Figure 4(a,b) shows the XP spectra of *w*-TiO$_2$ and *g*-TiO$_2$, respectively, in the Ti 2p BE region. The XPS Ti 2p peak was deconvoluted into two Ti 2p peaks at 458.57 and 464.27 eV for *w*-TiO$_2$, whereas the peaks were observed at 458.42 and 464.10 eV for *g*-TiO$_2$ nanoparticles, which were attributed to the splitting of Ti into Ti 2p$^{3/2}$ and Ti 2p$^{1/2}$ [7,41,42]. Both Ti 2p$^{3/2}$ and Ti 2p$^{1/2}$ peaks shifted towards a lower binding energy in the case of *g*-TiO$_2$, which confirms the modification and formation of Ti^{3+} in the TiO$_2$ nanostructure in MFC setup. Similarly, Zhao *et al.*[43], also reported that lower shift of Ti 2p BE is due to the formation of Ti^{3+} in TiO$_2$ lattices. The amount of Ti^{3+} on the TiO$_2$ surface plays a significant role, as described in the case of TiO$_2$ doped with metal atoms. The photogenerated electrons can be confined in Ti^{3+}, thus preventing the recombination rate of majority and minority carriers[43]. To control the binding states of oxygen in *w*-TiO$_2$ and *g*-TiO$_2$, the O 1 s XPS peak was fitted to three peaks (Fig. 4(c),(d)) cantered at 530.52, 532.22, and 528.06 eV for *w*-TiO$_2$ and 530.62, 531.92, and 529.68 eV for *g*-TiO$_2$ [6,42–44]. The shift in the O 1 s BE of *g*-TiO$_2$ compared to *w*-TiO$_2$ specifies a modification in the form of oxygen bonding, which is associated to the creation of Ti^{3+} [8]. The photoelectron peak sat around 530.62 and 529.68 eV were allocated to the lattice oxygen in TiO$_2$ and Ti$_2$O$_3$, correspondingly, however the peak at 531.92 eV was allotted to the water adsorbed on the TiO$_2$ surface (Fig. 4).

The reduction in the band gap may take place through the development of mid-gap band states whichever below the conduction band (CB) or above the valence band (VB) overlying with the respective bands. Therefore, VB XPS of the *w*-TiO$_2$ and *g*-TiO$_2$ nanoparticles was achieved to observe the band gap reduction phenomenon (Fig. 5(a)). The VB maximum of *w*-TiO$_2$ was detected at 1.76 eV, whereas the VB maximum of the *g*-TiO$_2$ was observed at 1.02 eV, showing a 0.74 eV shifts to a lower binding energy[6,18,45]. This shift was assigned to surface oxygen vacancies, Ti^{3+} formation and/or disorderliness in accordance with the TEM result and several other recent reports[6,18,21,28]. In particular, the band gap reduction caused by a lowering of CB was reported due to defects, such as oxygen vacancies and Ti^{3+} formation, which is related mainly to oxygen vacancies[2,16,18,28,45]. Chen *et al.* reported such an increase in the VB, which was due mainly to the existence of a disorder shell in the
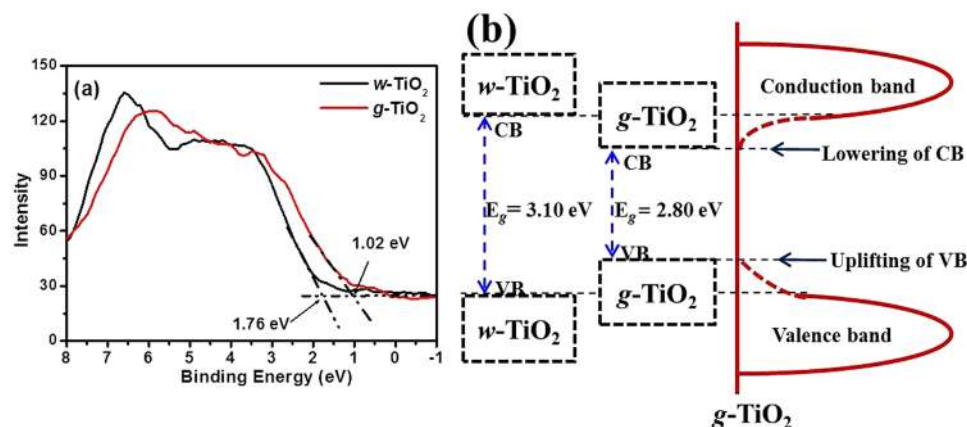
Figure 5. (**a**) VB of the *w*-TiO$_2$ and *g*-TiO$_2$ nanoparticles, and, (**b**) Proposed DOS for the *g*-TiO$_2$ nanoparticles.
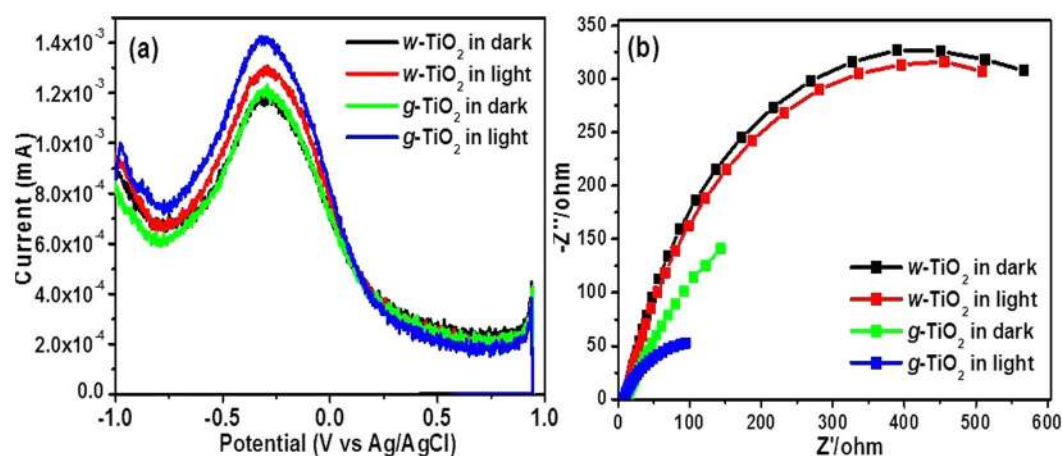

Figure 6. (**a**) DPV and (**b**) EIS of the *w*-TiO$_2$ and *g*-TiO$_2$ nanoparticles.

hydrogenated black TiO$_2$ nanoparticles[6]. The reduction of the band gap in the *g*-TiO$_2$ case was attributed to both the dropping of CB (due to oxygen vacancies and Ti^{3+} defect centres) and the increase in the VB (due to surface disorderliness)[2,6,16,18,28].

Based on the VB XPS results (Fig. 5(a),(b) presents a schematic illustration of the density of states (DOS) of disorder-engineered *g*-TiO$_2$ nanoparticles compared to those of unmodified *w*-TiO$_2$ nanoparticles. A measured band gap of 3.10 eV indicates a negligible change in the band edges of *w*-TiO$_2$. The *w*-TiO$_2$ displayed the typical VB DOS characteristics of TiO$_2$, with the edge of the maximum energy at approximately 1.76 eV. Therefore, the CB minimum would occur at ~1.50 eV. For *g*-TiO$_2$, the VB maximum energy showed a blue-shift toward the vacuum level at ~1.02 eV. A lower band gap from the DRS measurement for the *g*-TiO$_2$ and VB XPS shift was due to the surface disorder produced after the MFC treatment. In addition, there may be CB tail states arising from the defects (Ti^{3+}) that extend below the conduction band minimum[2,6,16,18,28]. The optical transitions from the blue-shifted VB edge to the band tail states are apparently responsible for optical absorption in *g*-TiO$_2$. This assumption was supported by DRS observations. An additional potential advantage of this engineered and disordered *g*-TiO$_2$ is that such defected and disordered metal oxides provide trapping sites (such as Ti^{3+}) for photogenerated carriers and inhibit them from rapid recombination, thereby enhancing electron transfer and photocatalytic reactions[21,29,30] (Fig. 5).

Photoelectrochemical studies. DPV is generally used to determine the charge storage capability of nanomaterials and is used frequently as a complementary technique to cyclic voltammetry. DPV was performed to understand the charge storage capability and the quantized behaviours of the *w*-TiO$_2$ and *g*-TiO$_2$ nanoparticles[46–49]. Figure 6a shows the well-defined quantized capacitance charging peaks for the *w*-TiO$_2$ and *g*-TiO$_2$ nanoparticles in the dark and under visible light irradiation. The peak current for *w*-TiO$_2$ and *g*-TiO$_2$ nanoparticles in the dark was observed at 1.170 mA and 1.218 mA, whereas it was observed at 1.290 mA and 1.416 mA under visible light, respectively. An increase in the peak current of 0.126 mA was observed in the case of *g*-TiO$_2$ nanoparticles under visible light irradiation. For the peak potential of *w*-TiO$_2$ and *g*-TiO$_2$ nanoparticles, no shift was observed. The increase in the peak current (0.126 mA) clearly shows the enhancement in the photoelectrochemical activity of *g*-TiO$_2$ nanoparticles compared to the *w*-TiO$_2$ nanoparticles, which may be due to the different
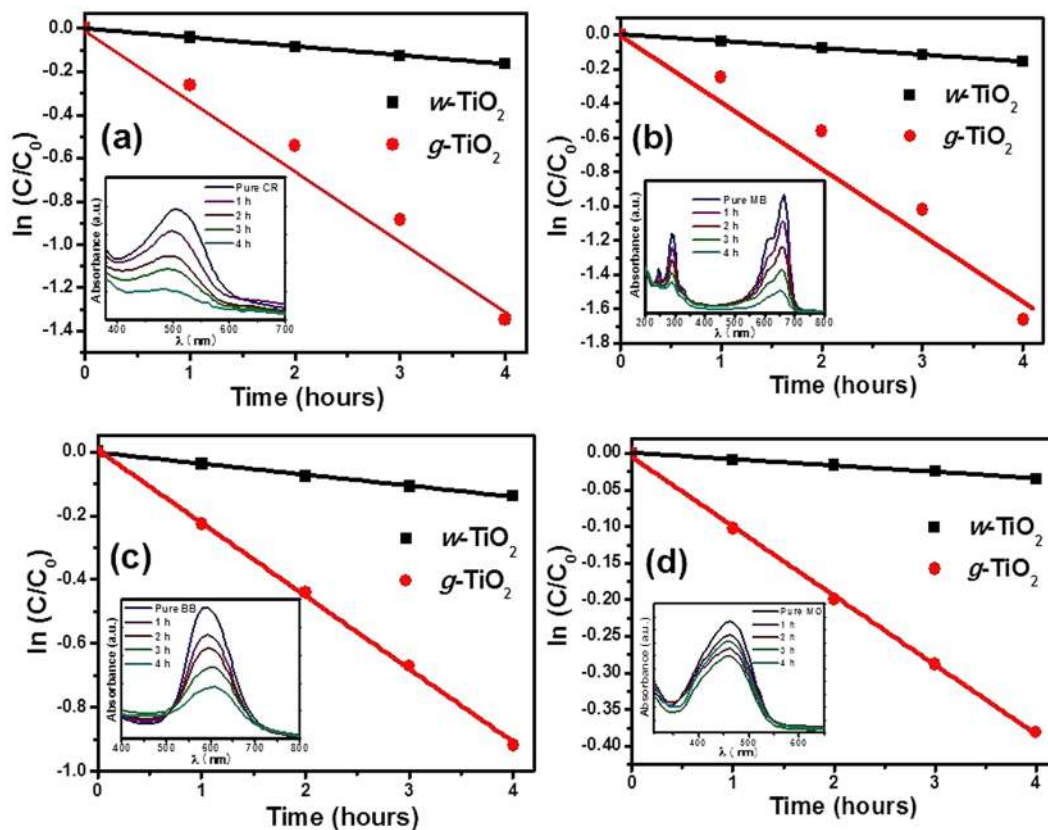
Figure 7. Visible light assisted photocatalytic degradation of (**a**) CR, (**b**) MB, (**c**) BB, and, (**d**) MO in the presence of the *w*-TiO$_2$ and *g*-TiO$_2$ nanoparticles.

types of defects formed in *g*-TiO$_2$ nanoparticles. The *g*-TiO$_2$ nanoparticles under visible light irradiation exhibited excellent and enhanced charge storing properties compared to *w*-TiO$_2$ nanoparticles. The electrons stored on the *g*-TiO$_2$ nanoparticles could be used to form different oxidative species (O$_2$$^{\bullet}$ and $^{\bullet}$OH) under visible light irradiation. These highly oxidative species might be responsible for degradation and mineralization of the organic colored dyes[21,29,30]. In addition, these stored electrons can be used for different photoactive devices. Overall, the *g*-TiO$_2$ nanoparticles could be a good photoelectrocatalyst for electron transfer reactions such as photocatalysis and optoelectronic devices (Fig. 6).

Generally, EIS is used to examine the electrochemical properties of the materials; hence, it was performed to understand the charge transfer resistance and charge separation efficiency between the photogenerated electrons and holes in the *w*-TiO$_2$ and *g*-TiO$_2$ nanoparticles. The charge separation efficiency of photogenerated electrons and holes is a critical factor for the photoelectrode and photocatalytic activities[50–52]. Figure 6b shows EIS Nyquist plots of the *w*-TiO$_2$ and *g*-TiO$_2$ nanoparticles in the dark and under visible light irradiation. The arc radius of the EIS spectra reflects the interface layer resistance arising at the electrode surface[50]. A smaller arc radius indicates higher charge transfer efficiency[21,50–52]. The arc radius of the *g*-TiO$_2$ nanoparticles was smaller than that of *w*-TiO$_2$ nanoparticles in the dark and under visible light irradiation. This suggests that the *g*-TiO$_2$ nanoparticles have a lower resistance than *w*-TiO$_2$ nanoparticles, which can accelerate the interfacial charge-transfer processes. These observations are supported by the PL results. EIS further support the important role of Ti^{3+} and different types of defects and oxygen vacancies, which help improve the charge separation (electrons and holes) and transfer efficiency of photogenerated electrons and holes on the surface of the *g*-TiO$_2$ nanoparticles compared to the *w*-TiO$_2$ nanoparticles in the dark and under visible light irradiations.

Visible light induced photocatalytic studies. The visible light-induced photocatalytic activities of the *w*-TiO$_2$ and *g*-TiO$_2$ nanoparticles were estimated by degrading CR, MB, BB and MO under the visible light ($\lambda > 500$ nm) as reported earlier[13,21,29,36,50]. The *g*-TiO$_2$ nanoparticles showed better photocatalytic degradation of CR, MB, BB, and MO than *w*-TiO$_2$ (Fig. 7). The visible light-induced photocatalytic degradation was estimated from the decrease in the absorption intensity of CR, MB, BB and MO at a fixed wavelength, $\lambda_{max} = 492$ nm, 665 nm, 588 nm, and 465 nm, respectively, during the course of the visible light-induced photocatalytic degradation experiment. The degradation was calculated using the relationship, ln C/C$_0$ vs time (h) where C$_0$ is the initial concentration and C is the concentration after visible light irradiation and degradation (Fig. 7). Inset of Fig. 7a,b,c, and d shows the respective decrease in absorbance after degradation. In addition, the degradation rate was also calculated to evaluate the precise degradation ability of the *w*-TiO$_2$ and *g*-TiO$_2$ nanoparticles. The rate constant (k) for the degradation of CR were 0.00072/h and 0.0570/h for *w*-TiO$_2$ and *g*-TiO$_2$ respectively, whereas
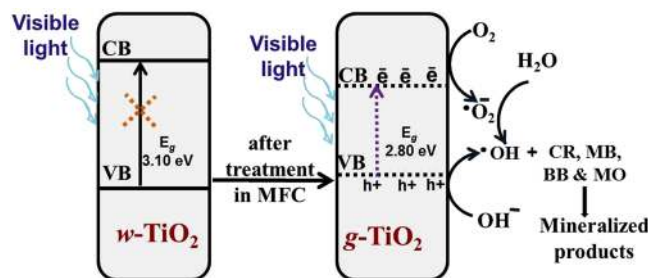
Figure 8. Proposed mechanism for the photocatalytic degradation of the dyes under visible light irradiation in the presence of *g*-TiO$_2$ nanoparticles.

0.0018/h and 0.1203/h for degradation of MB by *w*-TiO$_2$ and *g*-TiO$_2$, respectively. Similarly, the k value for the degradation of BB was 0.0028/h and 0.02284/h for *w*-TiO$_2$ and *g*-TiO$_2$ respectively, whereas it was 0.0003/h and 0.0048/h for degradation of MO by *w*-TiO$_2$ and *g*-TiO$_2$, respectively. These results clearly show that *g*-TiO$_2$ has higher k values for the degradation of CR, MB, BB, and MO compared to *w*-TiO$_2$. The enhanced photocatalytic activity of the *g*-TiO$_2$ nanoparticles compared to *w*-TiO$_2$ can be explained by the surface modification and defects in *g*-TiO$_2$ nanoparticles. Oxygen vacancies, other defects and Ti^{3+} centers enhance the photocatalytic activity[21,29]. The variation in the photocatalytic activity of *w*-TiO$_2$ and *g*-TiO$_2$ nanoparticles is also supported by DRS (Fig. 2(c)), EPR (Fig. 2b), and XPS (Figs 4 and 5). These outcomes evidently show that the visible light-induced photocatalytic performance of *g*-TiO$_2$ nanoparticles can be amended greatly by reduction the band gap and making various defects and Ti^{3+} centers[4–9,21,29] (Fig. 7).

Figure 8 shows the proposed schematic mechanism for the Ti^{3+} and oxygen vacancy-induced visible light photocatalytic degradation of the colored dyes (CR, MB, BB, and MO) in the presence of *g*-TiO$_2$ nanoparticles. The concept of heterogeneous photocatalysis is based on the ability of photocatalysts to harvest light energy that is required to generate electron–hole pairs for surface reactions. On the other hand, owing to the wide band gap of TiO$_2$, it can only absorb UV light. Fortunately, the optical properties of TiO$_2$ can be manipulated by defect engineering[4–9,13,21,29]. By introducing oxygen vacancies and other defects, the light absorption of TiO$_2$ from UV can be extended to the visible region of the spectrum because the oxygen vacancies give rise to the local states below the conduction band edge. The as-formed oxygen vacancy states can participate in a new photoexcitation process. That is, the electron is excited to the oxygen vacancy states from the valence band with the energy of visible light, which gives rise to typical excitations in the visible region of the spectrum. For this reason, oxygen vacancies are called F centers[21]. In addition, the electrons remaining in the oxygen vacancies can also interact with the adjacent Ti^{4+} to give the Ti^{3+} species. The Ti^{3+} defects can also form a shallow donor level just below the conduction band, which can also contribute to the visible light response[8]. The enhancement in the performance of *g*-TiO$_2$ was attributed to the high separation efficiency of e$^-$/h$^+$ pairs due to (Fig. 8) surface oxygen-vacancies and Ti^{3+} formation, which lead to band gap narrowing[4,5,21,26,29]. This band gap narrowing in *g*-TiO$_2$ nanoparticles provides the visible light-induced photocatalytic activity. Band gap excitation of the semiconductor consequences in e$^-$/h$^+$ separation. The high oxidative potential of the holes in the photocatalyst permits the formation of reactive intermediates[21,29]. Reactive hydroxyl radicals ($^{\bullet}$OH) can be shaped either by the decay of water or by the reaction of a hole with OH$^-$. The hydroxyl radicals and photogenerated holes are particularly strong, non-selective oxidants that prime to the degradation of CR, MB, BB, and MO at the surface of the *g*-TiO$_2$ nanoparticles[4,5,21,29,30]. This can be accredited to the high concentration of oxygen vacancies, other defects, and Ti^{3+} centers formed in the *g*-TiO$_2$ nanoparticles[21,29,38–45] (Fig. 8).

In general, high temperature, pressure, and energy input are required during synthesis and modification of nanomaterials[4–9]. On the other hand, in this proposed method, the modification process was quite efficient because there was no any external energy input except mechanical stirring and modification process took place at room temperature under atmospheric pressure. During the TiO$_2$ modification process in cathode of MFC, power density increased from 54.88 mW/m^2 to 70.39 mW/m^2 which is a big accomplishment[29]. There are few reports in which various types of materials have been used in cathode for the production of electricity with a high power density. For example, Han et al.[53], reported simultaneous degradation of pollutants and power generation in a MFC, where gold nanoparticles acted as a catalyst. The authors reported that a 36.56 mW/m^2 power density was achieved after complete removal of the pollutant. Therefore, in this study, the less expensive TiO$_2$, which was modified for visible light photocatalytic applications without any energy input, was used as the cathode catalyst.

Conclusions

A novel and biogenic method was used to modify the commercial TiO$_2$ nanoparticles (*w*-TiO$_2$) under ambient conditions, which resulted in an enhancement in their visible light assisted photocatalytic activities and photoelectrochemical behaviour. No structural changes occurred in *g*-TiO$_2$, but Ti^{3+} formation, oxygen vacancies, and surface defects were identified. EIS and LSV in the dark and under visible light irradiation confirmed the visible light-induced photoactivity of the *g*-TiO$_2$. Ti^{3+} and oxygen vacancy-induced visible light photocatalytic degradation of CR, MB, BB, and MO confirmed the improved photoactivity of the *g*-TiO$_2$. This study suggests that *g*-TiO$_2$ can be used as a visible light active photocatalyst as well as materials for photoelectrode. The MFC treatment can be employed to modify other metal oxides for enhanced visible light assisted photocatalytic activities and photoelectrochemical studies.

Experimental procedures

Materials used. TiO$_2$ nanoparticles (size < 25 nm), methylene blue (MB), and brilliant blue (BB) were purchased from Sigma-Aldrich. Methyl orange (MO), Congo red (CR), and sodium sulphate were acquired from Duksan Pure Chemicals Co. Ltd. South Korea. Ethyl cellulose and α-terpineol were provided by KANTO Chemical Co., Japan and fluorine-doped transparent conducting oxide glass (FTO; F-doped SnO$_2$ glass; 7 Ω/sq) was attained from Pilkington, USA. Altogether chemicals were of analytical grade and used as received. De-ionized water was prepared using a PURE ROUP 30 water purification system.

Methods

UV-Vis diffuse reflectance/absorbance spectroscopy (DRS) of the powdered w-TiO$_2$ and g-TiO$_2$ nanoparticles was performed using an ultraviolet – visible – near infrared (UV-VIS-NIR) double beam spectrophotometer (VARIAN, Cary 5000, USA) equipped with a diffuse reflectance accessory. A He-Cd laser (Kimon, 1 K, Japan) with a wavelength of 325 nm and a power of 50 mW was used as the excitation source for the photoluminescence (PL) measurements. X-ray diffraction (XRD, PANalytical, X'pert PRO-MPD, The Netherlands) was performed using Cu Kα radiation (λ = 0.15405 nm). A Rietveld refinement was conducted using Muad 2.46 software. Raman spectroscopy was performed on a HR800 UV Raman microscope (Horiba Jobin-Yvon, France). The electron paramagnetic resonance (EPR) measurements were performed using a Bruker EMX system. X-ray photoelectron spectroscopy (XPS, ESCALAB 250 XPS System, Thermo Fisher Scientific U.K.) was conducted using the following X-ray source: monochromated Al Kα, hν = 1486.6 eV, X-ray energy: 15 kV, 150 W and spot size: 500 μm. The XP spectra were fitted using the "Avantage program". The microstructures of the w-TiO$_2$ and g-TiO$_2$ were observed by high resolution transmission electron microscopy (HRTEM, JEM-2100 JEOL) at an operating voltage of 200 kV combined with energy dispersive spectrometry (EDS) and a high angle annular dark field STEM (HAADF-STEM). The selected-area electron diffraction (SAED) images were recorded on a HRTEM instrument. The photocatalytic degradation and photoelectrochemical experiments (EIS and LSV) were conducted using a 400 W lamp with an irradiating intensity of 31.0 mWcm^{-2} (3 M, USA). The electrochemical impedance spectroscopy (EIS) and linear scan voltammetry (LSV) measurements were carried out using a potentiostat (Versa STAT 3, Princeton Research, USA) with a standard three-electrode system, in which Ag/AgCl (3.0 M KCl), a Pt gauge and fluorine-doped tin oxide (FTO) glass coated with p-TiO$_2$, or m-TiO$_2$ were used as the reference, counter, and working electrodes, respectively, in a 0.2 M Na$_2$SO$_4$ solution as the electrolyte. The working electrodes, with an effective area of 0.64 cm^2, for EIS and LSV were prepared as follows. A 100 mg sample of each was suspended thoroughly by adding ethyl cellulose as a binder and α-terpineol as a solvent. The sample was mixed thoroughly for approximately 4 h and stirred at 50 °C for 4 h to obtain the paste. The obtained paste was coated on a FTO glass using the doctor-blade method, dried under a lamp for 24 h and used as the working electrode.

Modification of TiO2 nanoparticles in Microbial Fuel Cell.

Commercial TiO$_2$ nanoparticles were modified in the cathode of the MFC. The MFC was setup as reported elsewhere[53]. A 200 mL aqueous dispersion of w-TiO$_2$ (50 mM) was prepared in the cathode chamber of the MFC. The preliminary pH of the aqueous dispersions was 4.40. The MFC setup was run for 20 days. After modification, the final pH of the aqueous dispersion was 3.65. The almost white w-TiO$_2$ changed to a light gray colour upon modification. The resultant dispersion was centrifuged and a greyish powder was obtained, dried in an oven at 80 °C for 24 h and used in the different characterization techniques and applications.

Before and during the modification process, the voltage generated by the MFC was monitored regularly and recorded using a computerized multimeter. After stabilizing the MFC, the voltage obtained was ~0.3514 V and after the modification of TiO$_2$ in the MFC cathode, the voltage obtained was ~0.3979 V, which corresponds to a power density of 54.88 mW/m^2 and 70.39 mW/m^2, respectively.

Photoelectrochemical studies of the w-TiO2 and g-TiO2 nanoparticles.

To observe the photoelectrode performance of the w-TiO$_2$ and g-TiO$_2$ nanoparticles, photoelectrochemical experiments, such as EIS and LSV, were conducted under ambient conditions in the dark and under visible light irradiation in a 50 mL, 0.2 M Na$_2$SO$_4$ aqueous solution at room temperature. For each electrode, EIS was first performed in the dark and later under visible light irradiation (λ > 500 nm) at 0.0 V with frequencies ranging from 1–10^4 Hz. The photocurrent performance was attained by LSV in the dark and under visible light irradiation at a scan rate of 50 mV/s over the potential range, −1.0 to 1.0 V.

Photocatalytic degradation of CR, MB, BB and MO using w-TiO2 and g-TiO2 nanoparticles.

The photocatalytic performance of the w-TiO$_2$ and g-TiO$_2$ nanoparticles were confirmed for the photocatalytic degradation of CR (10 mg/L), MB (10 mg/L), BB (10 mg/L), and MO (10 mg/L), as reported elsewhere[21,29]. For the photodecomposition experiment, a 3.0 mg sample of each photocatalyst was suspended in 20 mL of the aqueous CR, MB, BB, and MO solutions. Every single solution was sonicated for 5 min and then stirred in the dark for 10 min to complete the adsorption and desorption equilibrium on the w-TiO$_2$ and g-TiO$_2$ nanoparticles. The solutions were irradiated with a 400 W lamp (λ > 500 nm) and the distance between the light source and dye solution was 25 cm. The four sets of experiments for CR, MB, BB, and MO degradation were observed for 4 h. The rates of CR, MB, BB, and MO degradation were examined by taking 1.7 mL of the samples from each set at every 1 h, centrifuging the degraded solution to remove the catalyst and recording the UV-vis spectra, from which the degradation of CR, MB, BB, and MO could be calculated.

As a control experiment, the w-TiO$_2$ nanoparticles (reference photocatalyst, Sigma-Aldrich) were used to degrade CR, MB, BB, and MO under the similar experimental conditions. Every single degradation experiment was executed in triplicate to ensure the photocatalytic activity of the w-TiO$_2$ and g-TiO$_2$ nanoparticles. The stability and reusability of the g-TiO$_2$ nanoparticles were also tested in a similar way to that stated above.

References

1. Fujishima, A. Electrochemical photolysis of water at a semiconductor electrode. *Nature* **238**, 37–38 (1972).
2. Hu, Y. H. A highly efficient photocatalyst—hydrogenated black TiO₂ for the photocatalytic splitting of water. *Angewandte Chemie International Edition* **51**, 12410–12412 (2012).
3. Chen, H., Nanayakkara, C. E. & Grassian, V. H. Titanium dioxide photocatalysis in atmospheric chemistry. *Chemical Reviews* **112**, 5919–5948 (2012).
4. Pelaez, M. *et al.* A review on the visible light active titanium dioxide photocatalysts for environmental applications. *Applied Catalysis B: Environmental* **125**, 331–349 (2012).
5. Hashimoto, K., Irie, H. & Fujishima, A. TiO₂ photocatalysis: a historical overview and future prospects. *Japanese journal of applied physics* **44**, 8269 (2005).
6. Chen, X., Liu, L., Peter, Y. Y. & Mao, S. S. Increasing solar absorption for photocatalysis with black hydrogenated titanium dioxide nanocrystals. *Science* **331**, 746–750 (2011).
7. Liu, G. *et al.* A red anatase TiO₂ photocatalyst for solar energy conversion. *Energy & Environmental Science* **5**, 9603–9610 (2012).
8. Pan, X., Yang, M.-Q., Fu, X., Zhang, N. & Xu, Y.-J. Defective TiO₂ with oxygen vacancies: synthesis, properties and photocatalytic applications. *Nanoscale* **5**, 3601–3614 (2013).
9. Zhu, Q. *et al.* Stable blue TiO₂₋ₓ nanoparticles for efficient visible light photocatalysts. *Journal of Materials Chemistry A* **2**, 4429–4437 (2014).
10. Asahi, R., Morikawa, T., Ohwaki, T., Aoki, K. & Taga, Y. Visible-light photocatalysis in nitrogen-doped titanium oxides. *Science* **293**, 269–271 (2001).
11. Khan, M. M., Adil, S. F. & Al-Mayouf, A. Metal oxides as Photocatalysts. *Journal of Saudi Chemical Society* **19**, 462–464 (2015).
12. Khan, S. U., Al-Shahry, M. & Ingler, W. B. Efficient photochemical water splitting by a chemically modified n-TiO₂. *Science* **297**, 2243–2245 (2002).
13. Khan, M. M., Ansari, S. A., Amal, M. I., Lee, J & Cho, M. H. Highly visible light active Ag@TiO₂ nanocomposites synthesized using an electrochemically active biofilm: a novel biogenic approach. *Nanoscale* **5**, 4427–4435 (2013).
14. Choudhury, B., Dey, M. & Choudhury, A. Defect generation, dd transition, and band gap reduction in Cu-doped TiO₂ nanoparticles. *International Nano Letters* **3**, 25 (2013).
15. Lee, J. S., You, K. H. & Park, C. B. Highly photoactive, low bandgap TiO₂ nanoparticles wrapped by graphene. *Advanced Materials* **24**, 1084–1088 (2012).
16. Yang, G., Jiang, Z., Shi, H., Xiao, T. & Yan, Z. Preparation of highly visible-light active N-doped TiO₂ photocatalyst. *Journal of Materials Chemistry* **20**, 5301–5309 (2010).
17. Tao, J., Luttrell, T. & Batzill, M. A two-dimensional phase of TiO₂ with a reduced bandgap. *Nature chemistry* **3**, 296–300 (2011).
18. Naldoni, A. *et al.* Effect of nature and location of defects on bandgap narrowing in black TiO₂ nanoparticles. *Journal of the American Chemical Society* **134**, 7600–7603 (2012).
19. Yin, W.-J. *et al.* Effective band gap narrowing of anatase TiO₂ by strain along a soft crystal direction. *Applied Physics Letters* **96**, 221901 (2010).
20. Santara, B., Giri, P., Imakita, K. & Fujii, M. Evidence for Ti interstitial induced extended visible absorption and near infrared photoluminescence from undoped TiO₂ nanoribbons: an *in situ* photoluminescence study. *The Journal of Physical Chemistry C* **117**, 23402–23411 (2013).
21. Khan, M. M. *et al.* Band gap engineered TiO₂ nanoparticles for visible light induced photoelectrochemical and photocatalytic studies. *Journal of Materials Chemistry A* **2**, 637–644 (2014).
22. Khan, M. M., Kalathil, S., Lee, J.-T. & Cho, M.-H. Enhancement in the photocatalytic activity of Au@TiO₂ nanocomposites by pretreatment of TiO₂ with UV light. *Bulletin of the Korean Chemical Society* **33**, 1753–1758 (2012).
23. Liu, L., Peter, Y. Y., Chen, X., Mao, S. S. & Shen, D. Hydrogenation and disorder in engineered black TiO₂. *Physical Review Letters* **111**, 065505 (2013).
24. Chen, X. *et al.* Properties of disorder-engineered black titanium dioxide nanoparticles through hydrogenation. *Scientific Reports* **3**, 1510 (2013).
25. Teng, F. *et al.* Preparation of black TiO₂ by hydrogen plasma assisted chemical vapor deposition and its photocatalytic activity. *Applied Catalysis B: Environmental* **148**, 339–343 (2014).
26. Leshuk, T. *et al.* Photocatalytic activity of hydrogenated TiO₂. *ACS applied materials & interfaces* **5**, 1892–1895 (2013).
27. Wang, G. *et al.* Hydrogen-treated TiO₂ nanowire arrays for photoelectrochemical water splitting. *Nano letters* **11**, 3026–3033 (2011).
28. Xia, T. & Chen, X. Revealing the structural properties of hydrogenated black TiO₂ nanocrystals. *Journal of Materials Chemistry A* **1**, 2983–2989 (2013).
29. Kalathil, S., Khan, M. M., Ansari, S. A., Lee, J. & Cho, M. H. Band gap narrowing of titanium dioxide (TiO₂) nanocrystals by electrochemically active biofilms and their visible light activity. *Nanoscale* **5**, 6323–6326 (2013).
30. Liu, X. *et al.* Green synthetic approach for Ti³⁺ self-doped TiO₂₋ₓ nanoparticles with efficient visible light photocatalytic activity. *Nanoscale* **5**, 1870–1875 (2013).
31. Zuo, F. *et al.* Self-doped Ti³⁺ enhanced photocatalyst for hydrogen production under visible light. *Journal of the American Chemical Society* **132**, 11856–11857 (2010).
32. Young, R. Introduction to the Rietveld method. *The Rietveld Method* (1993).
33. Das, T. K., Ilaiyaraja, P., Mocherla, P. S., Bhalerao, G. & Sudakar, C. Influence of surface disorder, oxygen defects and bandgap in TiO₂ nanostructures on the photovoltaic properties of dye sensitized solar cells. *Solar Energy Materials and Solar Cells* **144**, 194–209 (2016).
34. Park, S.-J. *et al.* In situ control of oxygen vacancies in TiO₂ by atomic layer deposition for resistive switching devices. *Nanotechnology* **24**, 295202 (2013).
35. Arora, A. K., Rajalakshmi, M., Ravindran, T. R. & Sivasubramanian, V. Raman spectroscopy of optical phonon confinement nanostructured materials. *J. Raman. Spectrosc* **38**, 604–617 (2007).
36. Gouadec, G. & Colomban, P. Raman Spectroscopy of nanomaterials: How spectra relate to disorder, particle size and mechanical properties. *Prog. Cryst. Growth Charact. Mater* **53**, 1–56 (2007).
37. Chiesa, M., Paganini, M. C., Livraghi, S. & Giamello, E. Charge trapping in TiO₂ polymorphs as seen by Electron Paramagnetic Resonance spectroscopy. *Physical Chemistry Chemical Physics* **15**, 9435–9447 (2013).
38. Hoang, S., Berglund, S. P., Hahn, N. T., Bard, A. J. & Mullins, C. B. Enhancing visible light photo-oxidation of water with TiO₂ nanowire arrays via cotreatment with H₂ and NH₃: synergistic effects between Ti³⁺ and N. *Journal of the American Chemical Society* **134**, 3659–3662 (2012).
39. Jing, L. *et al.* Review of photoluminescence performance of nano-sized semiconductor materials and its relationships with photocatalytic activity. *Solar Energy Materials & Solar Cells* **90**, 1773–1787 (2006).
40. Kaniyankandy, S. & Ghosh, H. N. Efficient luminescence and photocatalytic behaviour in ultrafine TiO₂ particles synthesized by arrested precipitation. *Journal of Materials Chemistry* **19**, 3523–3528 (2009).
41. Chetri, P. & Choudhury, A. Investigation of optical properties of SnO₂ nanoparticles. *Physica E: Low-dimensional Systems and Nanostructures* **47**, 257–263 (2013).
42. Kim, H.-B. *et al.* Effects of electron beam irradiation on the photoelectrochemical properties of TiO₂ film for DSSCs. *Radiation Physics and Chemistry* **81**, 954–957 (2012).

43. Zhao, Z. *et al.* Reduced TiO₂ rutile nanorods with well-defined facets and their visible-light photocatalytic activity. *Chemical Communications* **50**, 2755–2757 (2014).
44. Etacheri, V., Seery, M., Hinder, S. & Pillai, S. Oxygen Rich Titania: A Dopant Free, A Dopant Free, High Temperature Stable, and Visible-Light Active Anatase Photocatalyst. (2011).
45. Kalathil, S., Lee, J. & Cho, M. H. Gold nanoparticles produced *in situ* mediate bioelectricity and hydrogen production in a microbial fuel cell by quantized capacitance charging. *ChemSusChem* **6**, 246–250 (2013).
46. Yang, A. *et al.* A simple one-pot synthesis of graphene nanosheet/SnO₂ nanoparticle hybrid nanocomposites and their application for selective and sensitive electrochemical detection of dopamine. *Journal of Materials Chemistry B* **1**, 1804–1811 (2013).
47. Khan, M. E., Khan, M. M. & Cho, M. H. CdS-graphene nanocomposite for efficient visible-light-driven photocatalytic and photoelectrochemical applications. *Journal of Colloid and Interface Science* **482**, 221–232 (2016).
48. Khan, M. M., Ansari, S. A., Lee, J. & Cho, M. H. Enhanced optical, visible light catalytic and electrochemical properties of Au@TiO₂ nanocomposites. *Journal of Industrial and Engineering Chemistry* **19**, 1845–1850 (2013).
49. Ansari, S. A. *et al.* Oxygen vacancy induced band gap narrowing of ZnO nanostructures by an electrochemically active biofilm. *Nanoscale* **5**, 9238–9246 (2013).
50. Bai, X. *et al.* Performance enhancement of ZnO photocatalyst via synergic effect of surface oxygen defect and graphene hybridization. *Langmuir* **29**, 3097–3105 (2013).
51. Gan, J. *et al.* Oxygen vacancies promoting photoelectrochemical performance of In₂O₃ nanocubes. *Scientific reports* **3**, 1021 (2013).
52. Khan, M. E., Khan, M. M. & Cho, M. H. Ce³⁺-ion, surface oxygen vacancy, and visible light-induced photocatalytic dye degradation and photocapacitive performance of CeO₂-Graphene nanostructures. *Scientific reports* **7**, 5928 (2017).
53. Han, T. H., Khan, M. M., Kalathil, S., Lee, J. & Cho, M. H. Simultaneous enhancement of methylene blue degradation and power generation in a microbial fuel cell by gold nanoparticles. *Industrial & Engineering Chemistry Research* **52**, 8174–8181 (2013).

Acknowledgements

Author Contributions

M.M. Khan and M.E. Khan planned the work, performed the experiments, analysed the results and wrote the manuscript. B.K. Min helps in the XRD and TEM analysis and its interpretation. M.H. Cho helps in planning the work, analysed the results and the writing manuscript.

Additional Information

Supplementary information accompanies this paper at https://doi.org/10.1038/s41598-018-19617-2.

Competing Interests: The authors declare that they have no competing interests.

Publisher's note: Springer Nature remains neutral with regard to jurisdictional claims in published maps and institutional affiliations.